Journal of Geophysical Research: Solid Earth

RESEARCH ARTICLE
10.1002/2017JB015252

Key Points:
- Variational Bayesian ICA provides optimal detection of hydrological deformation signals acting at different spatial scales and timing
- We highlight sequence of compression/extension strains normal to fractures in karst areas modulated by changes in the precipitation history
- Pressure changes associated with variable water levels in vertical fractures of karst aquifers explain deformation transients

Supporting Information:
- Supporting Information S1
- Data Set S1
- Data Set S2

Correspondence to:
E. Serpelloni,
enrico.serpelloni@ingv.it

Citation:
Serpelloni, E., Pintori, F., Gualandi, A., Scoccimarro, E., Cavaliere, A., Anderlini, L., et al. (2018). Hydrologically induced karst deformation: Insights from GPS measurements in the Adria-Eurasia plate boundary zone. *Journal of Geophysical Research: Solid Earth*, *123*, 4413–4430. https://doi.org/10.1002/2017JB015252

Received 28 NOV 2017
Accepted 19 MAR 2018
Accepted article online 24 MAR 2018
Published online 29 MAY 2018

Hydrologically Induced Karst Deformation: Insights From GPS Measurements in the Adria-Eurasia Plate Boundary Zone

E. Serpelloni[1], F. Pintori[2], A. Gualandi[3], E. Scoccimarro[4], A. Cavaliere[5], L. Anderlini[1], M. E. Belardinelli[2], and M. Todesco[5]

[1]Istituto Nazionale di Geofisica e Vulcanologia, Centro Nazionale Terremoti, Bologna, Italy, [2]Dipartimento di Fisica e Astronomia, Settore di Geofisica, Università di Bologna, Bologna, Italy, [3]Jet Propulsion Laboratory, California Institute of Technology, Pasadena, CA, USA, [4]Fondazione Centro euro-Mediterraneo sui Cambiamenti Climatici, Bologna, Italy, [5]Istituto Nazionale di Geofisica e Vulcanologia, Sezione di Bologna, Bologna, Italy

Abstract We apply a blind source separation algorithm to the ground displacement time series recorded at continuous Global Positioning System (GPS) stations in the European Eastern Alps and Northern Dinarides. As a result, we characterize the temporal and spatial features of several deformation signals. Seasonal displacements are well described by loading effects caused by Earth surface mass redistributions. More interestingly, we highlight a horizontal, nonseasonal, transient deformation signal, with spatially variable amplitudes and directions. The stations affected by this signal reverse the sense of movement with time, implying a sequence of dilatational and compressional deformation that is oriented normal to rock fractures in karst areas. The temporal evolution of this deformation signal is correlated with the history of cumulated precipitations at monthly time scales. This transient horizontal deformation can be explained by pressure changes associated with variable water levels within vertical fractures in the vadose zones of karst systems. The water level changes required to open or close these fractures are consistent with the fluctuations of precipitation and with the dynamics of karst systems.

Plain Language Summary Groundwater levels in aquifers are commonly monitored at local scales by wells. Space geodesy, however, can provide measurements of time-variable deformation associated with variable groundwater levels at mesoscales. Here we show how Global Positioning System (GPS) time series from regional networks can precisely measure spatially integrated deformation signals related to variable water levels in karst aquifers, which are an important source of drinking water worldwide. Blind source separation algorithms, as the one used in this work, help scientists to detect and precisely measure ground displacements associated with both tectonic and nontectonic processes, improving our ability to describe the space and time evolution of surface movements and the dynamics of faults and geological bodies.

1. Introduction

Long-term strain accumulation, fault slip rates, and seismic activity along plate boundaries are mainly driven by plate tectonics. However, it has been shown that several surface and subsurface processes, both of natural and anthropogenic origin, can affect the long-term tectonic deformation and even modulate or trigger seismicity (e.g., Amos et al., 2014; Bettinelli et al., 2008; Hainzl et al., 2006). Geodetic methods are now commonly used to study load processes (e.g., ocean tide and atmospheric loading, changes in continental water storage, and ice and snow coverage), which mainly generate vertical displacements from millimeter to decimeter, with different spatial scales and periodicities (e.g., Chanard et al., 2014; Fu et al., 2013; Jiang et al., 2010; Wahr et al., 2013). The analysis of these signals is attracting more and more attention since accounting for these variations is important to accurately measure secular geodetic velocities (Blewitt & Lavallee, 2002) and to properly infer and accurately measure timing and amplitude of tectonic deformation transients, including those occurring in slowly deforming regions (e.g., Gualandi, Nichele, et al., 2017).

At local scale, the influence of rainfall on crustal deformation has been described using tilt and strain meters in several tectonic settings (e.g., Dal Moro & Zadro, 1998; Evans & Wyatt, 1984; Gilli et al., 2010; Jacob et al., 2010; Jahr et al., 2008; Kümpel et al., 1988; Takemoto, 1995). However, the literature on the spatial extent of rainfall-induced deformation is still scarce. Recently, Global Positioning System (GPS) data have evidenced horizontal and vertical displacements correlated with rainfall, superimposed on the long-term tectonic motion, in karst areas (e.g., Devoti et al., 2015; Moreau & Dauteuil, 2013). Devoti et al. (2015), in particular,

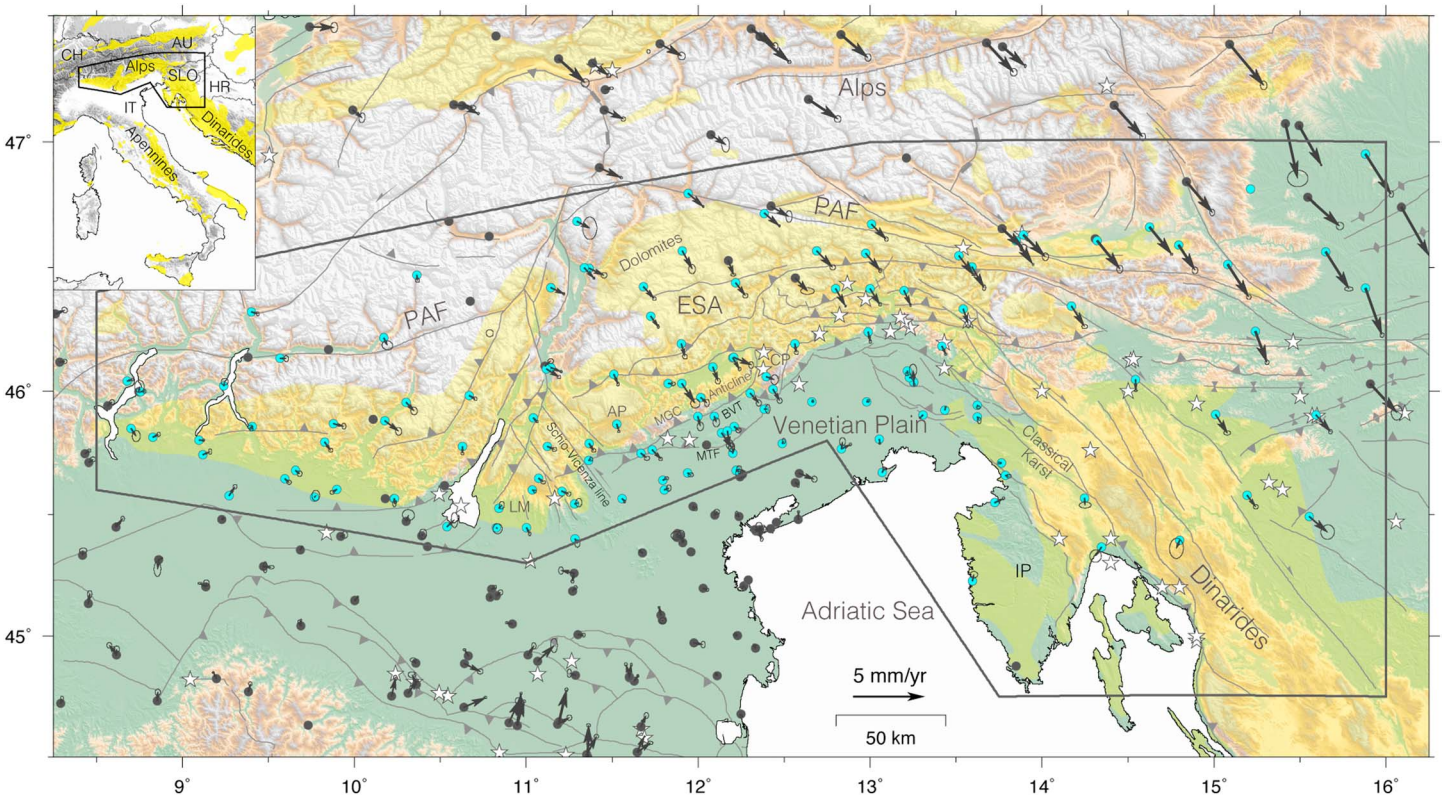

Figure 1. Map of the study region, showing in yellow areas where carbonate rocks outcrop (http://web.env.auckland.ac.nz/our_research/karst). The gray lines are faults from Serpelloni et al. (2016). The gray arrows show horizontal Global Positioning System velocities (with 95% error ellipses) in an Adria-fixed frame (from Serpelloni et al., 2016). The cyan circles indicate the Global Positioning System stations located within the black polygon and included in the time series analysis. The dark gray circles indicate stations excluded from the analysis because of short time series or large data gaps. The white stars indicate locations of $M > 5.5$ earthquakes from http://emidius.mi.ingv.it/CPTI15-DBMI15. ESA = Eastern Southern Alps; LM = Lessini Mountains; PAF = Periadriatic Fault; BVT = Bassano Valdobbiadene thrust fault; MTF = Montello thrust fault; AP = Asiago Plateau; CP = Cansiglio Plateau; IP = Istria peninsula; MGC Anticline = Monte Grappa-Monte Cesen anticline.

described a localized active slope deformation signal, highlighted by GPS and tiltmeter stations, in a karstic limestone plateau in the southeastern Alps (the Cansiglio Plateau, CP in Figure 1), which correlates with rainfall data. Silverii et al. (2016) discussed seasonal and multiyear deformation in GPS time series affecting a wider region, the southern Apennines of Italy, which have been associated with groundwater variations in karst aquifers. Karst systems appear thus ideal settings for investigating the effects of rainfall, rainwater infiltration, and changes in the water table on crustal deformation, potentially affecting the earthquake rates.

Large part of the tectonically active peri-Adriatic mountain belts (the Apennines-Alpine-Dinaric chain) is formed by limestone, characterized by diverse karstification levels. The same area is also characterized by a good coverage of continuous GPS (cGPS) networks (Devoti et al., 2017; Serpelloni et al., 2016). Since several tectonic and nontectonic processes are contributing to generate Earth's surface displacements (Dong et al., 2002), an accurate estimate of the ground deformation associated with the hydrological cycle would require the identification of the different deformation sources contributing to the ground displacements measured by GPS. Because different physical sources may have different temporal and spatial features, multivariate statistical analysis represent an efficient approach to address this problem and is now widely used (e.g., Amiri-Simkooei et al., 2017; Boergens et al., 2014; Dong et al., 2006; Ji & Herring, 2012). The identification of transient signals of nontectonic origin is even more important when transient tectonic deformations are expected to be smaller or of the same order of magnitude than hydrological deformation, thus making misinterpretation possible (e.g., Amoruso et al., 2017).

In this work, we applied a blind source separation algorithm to the position time series of cGPS stations operating in the area encompassing the Italian central and Eastern Southern Alps (ESA) and northern Dinarides in Slovenia and Croatia (see Figure 1). We adopted an approach that has been successfully used, in recent times, to separate both continental-scale hydrological signals from tectonic transients in several tectonic settings

(Gualandi, Avouac, et al., 2016; Gualandi, Perfettini, et al., 2017). The outputs of this analysis are the temporal evolution and the spatial response (i.e., the amplitude at each measuring station) of the individual signals contributing to the total observed geodetic ground displacements. After describing the geologic setting of the study region (section 2) and the data used (section 3), section 4 focuses on the individual signals obtained from the analysis carried out on de-trended position time series. Here we discuss the annual (seasonal) signals and present the analysis on a nonseasonal signal inducing a succession of extensional/compressional deformation. In section 5, this latter signal is correlated with precipitation data. Results are discussed in section 6, where we concentrate on the area with the highest density of GPS stations and develop a model to capture the first-order features of the displacement field. The successful exercise provides preliminary indication on the possible physical mechanism causing the time-variable strain observed in the karts sectors of the study area.

2. Geologic and Tectonic Settings

The Alps were developed from the Cretaceous onward by subduction of a Mesozoic ocean followed by collision between the Adriatic (Austroalpine-Southalpine) and European (Penninic-Helvetic) continental margins. The continent-continent collision started after the subduction and thrusting of the Penninic flysch units, during the Eocene (~50 Ma) (Decker & Peresson, 1996). According to the direction of tectonic transport, the Alps are subdivided into two belts of differing size, age and geological significance: (1) the Europe-verging belt, a thick collisional wedge of Cretaceous-Neogene age (~145–2.5 Ma), consisting of continental and minor oceanic units radially displaced toward the Molasse foredeep and European foreland; (2) the Southern Alps, a minor, shallower (nonmetamorphic) and younger (Neogene to present, ~23–0 Ma) thrust-and-fold belt displaced to the south (Adria verging), which developed within the Alpine hinterland of the Adriatic upper plate. The two belts are separated by the Periadriatic lineament or Periadriatic fault (see Figure 1), a major fault system of Oligocene-Neogene age (~34–2.5 Ma). The Dinaric Alps (or Dinarides) are part of the Alpine, Carpathian, Dinaric system (AlCaDi, after Schmid et al., 2008) and are a Late Jurassic to recent, mainly SW vergent fold-and-thrust belt that extends from the Southern Alps in the NW to the Albanides/Hellenides to the SE. The Eastern Alps and northern Dinarides (see Figure 1) marks the boundary between the Adriatic and the Eurasian plates through a wide zone of deformation including a variety of tectonic styles within a complex network of crustal and lithospheric faults (see Serpelloni et al., 2016, for a recent synoptic view). The large part of the Adria-Eurasia convergence is now accommodated across the southernmost ESA thrust front, where the highest geodetic strain rates are observed in its central segment (the Montello and Cansiglio thrusts; Danesi et al., 2015; Serpelloni et al., 2016; see Figure 1). Cheloni et al. (2014) and Serpelloni et al. (2016) showed that the ESA thrust front presents variable interseismic coupling, but uncertainties on coupling values, in particular for its central (i.e., Venetian) sector, are large, due to uncertainties in long-term motion rates of GPS sites located in the Cansiglio Plateau, which are affected by hydrological deformation transients (e.g., Devoti et al., 2015). Moreover, Serpelloni et al. (2016) have shown that GPS velocity gradients along the Adria-Eurasia convergence direction across the Montello-Cansiglio thrusts are difficult to be explained with elastic coupling models.

2.1. The South Alpine and Dinaric Karst

The Venetian Southern Alps, the southernmost sector of the Italian Eastern Alps, are composed by carbonate rocks, where the principal formations are well-bedded limestones of Jurassic age (the Calcari Grigi and the Rosso Ammonitico) that are overlaid by cherty or marly, more densely fractured, Cretaceous limestones (Maiolica formation, a chalk, and the Scaglia Variegata Alpina). The Dinarides are formed largely of Mesozoic and Cenozoic sedimentary rocks like dolomite, limestone, sandstone, and conglomerate. The study area is characterized by the presence of different karst massifs (see Figure 1), among which the most important ones are the Lessini Mountains, the Asiago Plateau and the Cansiglio Plateau along the Venetian Southern Alps front, and the Classical Karst, extending across the border between SW Slovenia and NE Italy, having a special place among karst regions in the world.

Karsts are found in widely scattered sections of the world (http://web.env.auckland.ac.nz/our_research/karst) and contain aquifers that are capable of providing large supplies of water, with more than 25% of the world's population either living on or obtaining its water from karst aquifers. Conditions that promote karst development are well-jointed limestone near the surface, a moderate to heavy rainfall and good groundwater

circulation. Karsts terrains are characterized by barren, rocky ground, caves, sinkholes, underground rivers, and the absence of surface streams and lakes, resulting from the excavating effects of underground water on soluble limestone. Rainwater quickly moves through the crevices into the ground, sometimes leaving the surface soil parched between rains. Karst aquifers are characterized by a network of conduits and caves, formed by chemical dissolution, allowing for rapid and often turbulent water flow, and may be present even when there are no discernible karst landforms at the land surface, and even when there are no known and accessible caves. An important way that karst aquifers differ from other aquifers is that a groundwater basin boundary may have little relationship to surface watershed boundaries. Recharge water may originate from the karst area itself or from adjacent nonkarstic areas, with infiltration occurring through the soil and unsaturated zone but being also concentrated via shallow holes/sinks and fractures. The properties of karst aquifers greatly vary in space and depend on the orientation of geologic fabric elements. Openings forming karst aquifers may be partly or completely water filled. The water tables in karst areas (i.e., the region where all pores are filled with water) can be highly irregular in elevation, because water-carrying conduits can develop at various elevations. Moreover, the water table in karst aquifers can sometimes fluctuate tens or even hundreds of meters even in relatively short periods of time (hours to days).

3. GPS Data and Time Series Analysis

The daily position time series of all cGPS networks operating in the study region (see Figure S1 in the supporting information for site locations and stations codes) were obtained analyzing the raw data with the GAMIT/GLOBK (Herring et al., 2015) and QOCA software (http://qoca.jpl.nasa.gov), following the three-step procedure described in Serpelloni et al. (2006, 2013). More details on the GPS data analysis are provided in the supporting information (Altamimi et al., 2011; Blewitt & Lavallee, 2002; Boehm et al., 2006; Dong et al., 2002, 2006; Herring et al., 2015; Lagler et al., 2013; Lyard et al., 2006; Petrie et al., 2010; Schmid et al., 2005, 2007; Serpelloni et al., 2006, 2013). A continental-scale common mode signal was estimated using principal component analysis, as in Serpelloni et al. (2013, 2016) and removed from the time series, bringing an increasing signal-to-noise ratio (SNR) in displacement time series.

The displacement time series of the stations located within the black polygon in Figure 1 were analyzed using the variational Bayesian independent component analysis (vbICA) method (Choudrey & Roberts, 2003), modified and tested on GPS position time series by Gualandi, Serpelloni, and Belardinelli (2016). The vbICA approach uses a generative model to recreate the observations. Every independent component (IC) is described by a mix of Gaussians (MoG), which allows for more flexibility in the description of the sources with respect to classical independent component analysis (ICA) techniques. The vbICA method carries with it other two advantages: first, it allows to consistently taking into account missing data in the data set (see Chan et al., 2003); second, it provides an estimate of the uncertainty associated with each IC. The output of this analysis is the definition of a limited number (L) of sources or components. Each source has a specific spatial distribution (U) and follows a specific temporal evolution (V). Both the spatial and temporal responses associated with every IC have unit norm, so that a weight coefficient S (in mm) is necessary to rescale their contribution in explaining the original data. The displacement time series at a given station can be reconstructed by linearly summing up the contributions from all the ICs, each of which is obtained by multiplying the specific spatial distribution by the associated weight times the temporal evolution. The probability density function (pdf) of each time function V_i, $i = 1, \ldots, L$, is modeled via a MoG. Given a sufficient number of Gaussians, any pdf can be reproduced by a MoG. The vbICA searches for the parameters of the MoG such that the pdfs of the temporal functions are as much independent as possible while being able to explain satisfactorily the observations. This data-driven approach allows extracting the spatiotemporal information of independent sources without imposing any specific spatial distribution or temporal function but extracting them directly from the observations.

We used de-trended time series, removing the linear trend estimated from the absolute (i.e., IGb08) time series, corrected for known offsets due to changes in stations equipment. Only stations with $>$3.5 years of data are retained in this analysis. Using de-trended time series reduces the correlation of the data set, improving the ability of the vbICA algorithm to correctly separate the sources (Gualandi, Serpelloni, & Belardinelli, 2016). In order to limit missing data, we removed from the analysis stations presenting large data gaps, obtaining a total coverage of 65%. The stations used are shown in cyan in Figure 1. The analysis yields that

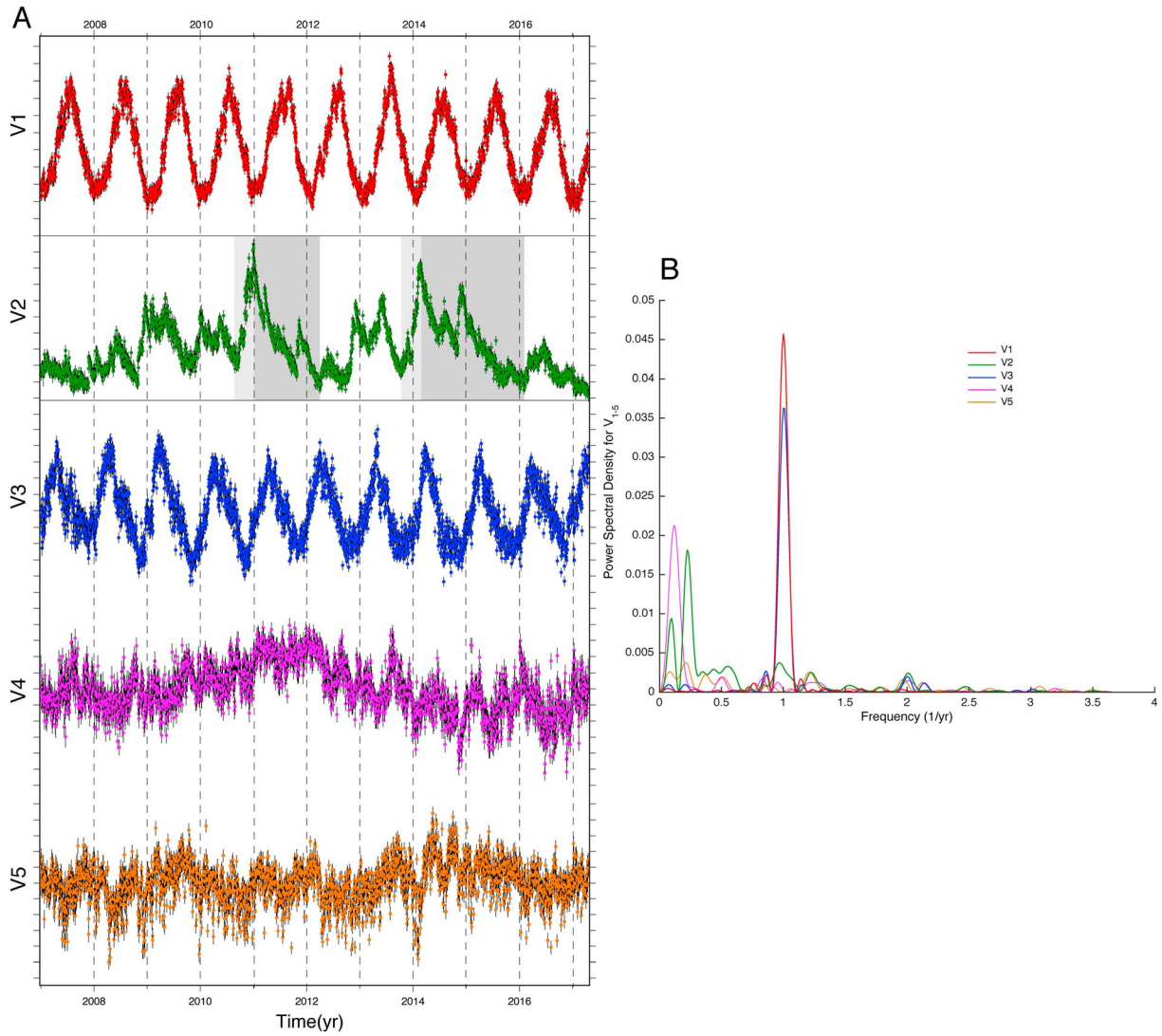

Figure 2. (a) Temporal evolution (*V*) of the five independent components determined from the variational Bayesian independent component analysis and (b) corresponding power spectral density plots, where the red, green, blue, purple, and orange symbols and lines refer to IC1, IC2, IC3, IC4, and IC5. Gray bars are one standard deviation errors.

five ICs are required to properly reconstruct the time series, where this number is based on the automatic relevance determination criterion and the estimation of the negative free energy associated with the generative model, as described in Gualandi, Serpelloni, and Belardinelli (2016).

4. ICA Results

4.1. ICs Temporal and Spatial Features

The temporal evolution (*V*) and the power spectral density of the five ICs are shown in Figure 2. Map views of the spatial response (*U*) corresponding to each IC and the associated weight (*S* in mm) are shown in Figure 3, where the color of circles and the length of the green arrows indicate the direction and the amplitude of *U* at each station in the vertical and horizontal components, respectively. The uncertainties on the IC are calculated following Gualandi, Avouac, et al. (2016) and might be underestimated since spatial and temporal correlations are neglected. For each station and each IC, we computed the SNR value as the ratio of the squared difference between the maximum and minimum displacements associated with each IC and the mean uncertainty (one standard deviation) of the GPS measurements. Figure S2 in the supporting information shows maps of the spatial response for the five ICs for the stations with SNR $>$ 1 at least in one of the

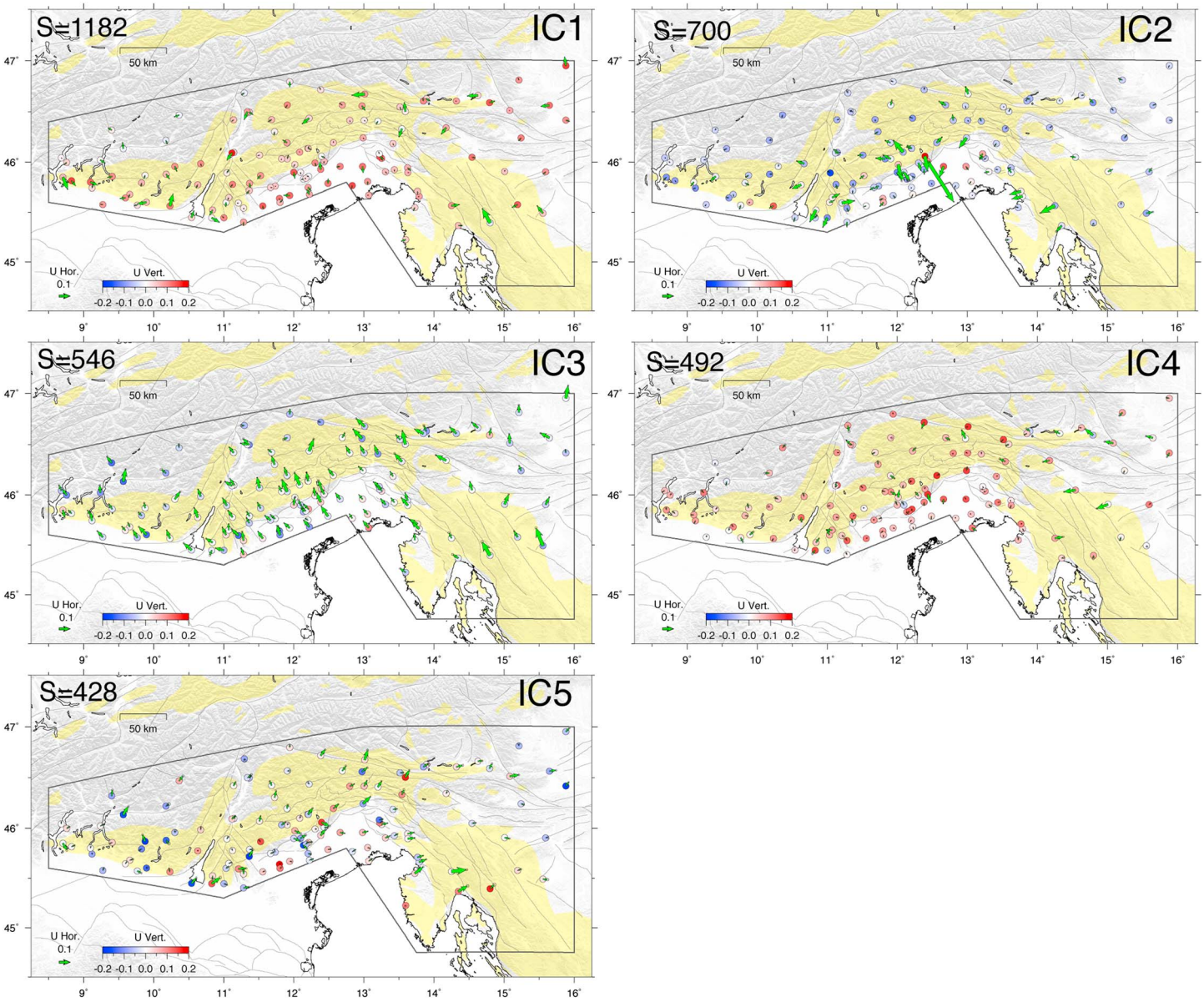

Figure 3. Map views of the spatial response, *U*, for the five independent components, where the green arrows show the horizontal response and the color scale refers to the vertical response. The weight *S* (in mm) for each independent component is shown in the upper left corner. The spatial response describes the directions along which the Global Positioning System station move and the arrow length, or color, is proportional to the importance of this specific component at each single station.

horizontal components or in the vertical one. For each IC the number of stations with SNR $>$ 1 provides an indication on how important is the single IC in describing the measured displacements time series.

The frequency analysis (Figure 2b) shows that the temporal evolution of the first and third ICs (V1 and V3) has peaks corresponding to annual signals, and the two annual signals have a phase lag of 96 ± 2 days, with V3 anticipating V1. V2 and V4 have more power at low frequencies, with V4 representing a multiyear signal. V2, in particular, combines different long-period signals with smaller power at annual and semiannual periods, displaying a noncyclic signal that varies in amplitude during the investigated time span. The time spans presenting larger variations of V2 are shown in gray in Figure 2a and correspond to the two time intervals later considered in this work for more in-depth study. During periods of rapid increase (light gray areas in Figure 2) the signal seems to have a linear trend, whereas during periods of decrease (dark gray areas in Figure 2), V2 shows a nonlinear behavior. V5 has significantly less power than the other ICs and no dominant peaks, suggesting that this component represents mainly noise in the GPS time series.

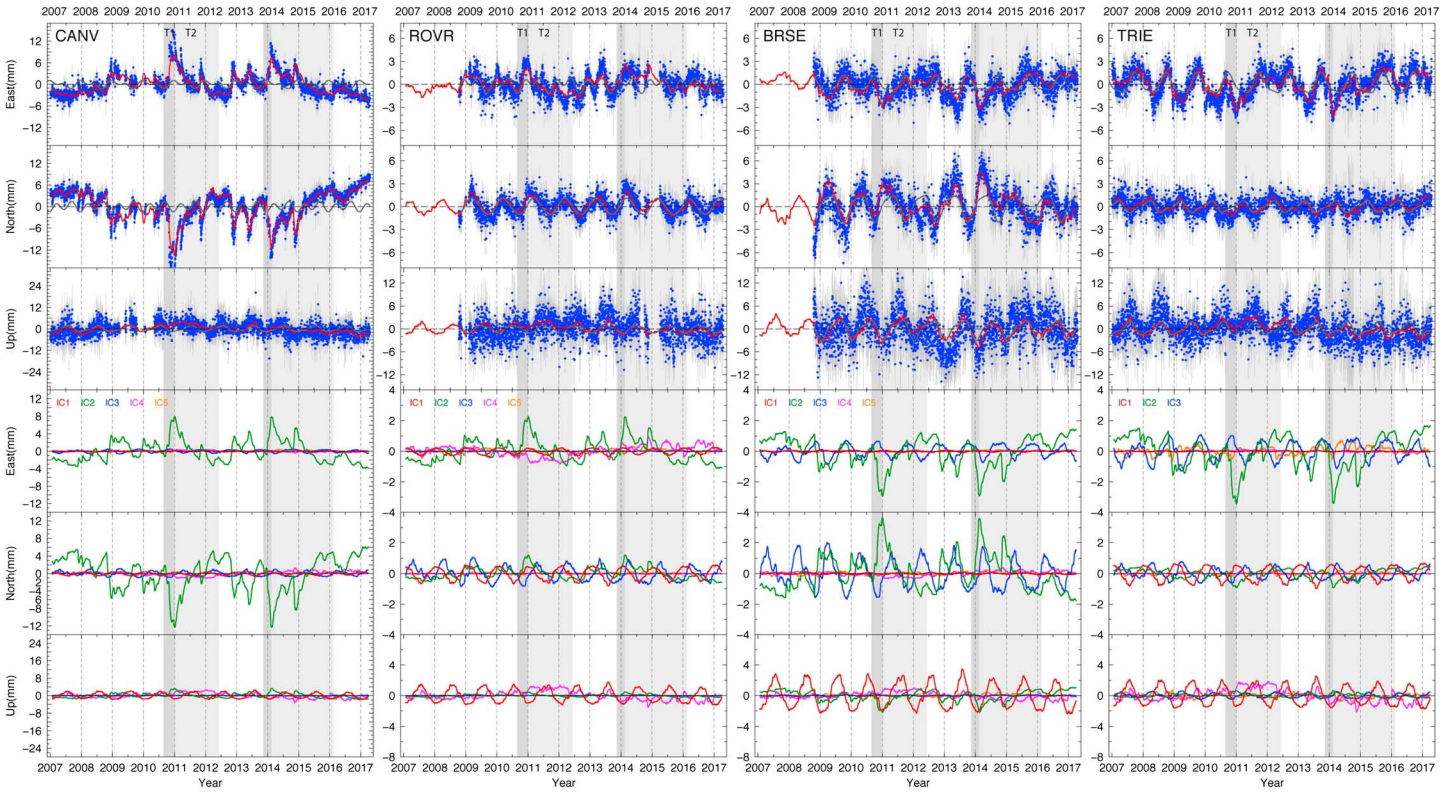

Figure 4. De-trended observed (blue dots) and reconstructed (red line) displacement time series obtained from the determined five independent components (ICs), for four Global Positioning System stations located in the three areas shown in Figure 6. The dark gray lines show fit to the observations with an annual + semiannual model obtained by least squares fit of the Global Positioning System observations using the QOCA analyze_tseri package (https://qoca.jpl.nasa.gov). The displacement time series associated with each of the five ICs are reported in the bottom panels with different colors. The gray areas indicate time intervals where the cumulative displacements associated with the second IC are larger.

In terms of spatial response (shown in Figure 3), IC1 and IC3 look like common mode signals, with stations moving at annual periods coherently in the same direction; for IC1 mostly up and down and for IC3 mostly NW-SE, since no stations have SNR $>$ 1 in the vertical components for IC3, while for IC1 the direction at sites with SNR $>$ 1 in the horizontal (see Figure S2) is variable. IC2, on the contrary, shows a more heterogeneous spatial response in the horizontal component, with high SNR at stations located in the Southern Alps and northern Dinarides (see Figure 6). On the other hand, only very few sites have SNR $>$ 1 in the vertical component for IC2. For IC4 and IC5 only 1–10% of sites have SNR $>$ 1 and marginally contribute in describing the measured displacements at very few stations.

Figure 4 shows the observed (in blue) and reconstructed (in red) time series for four stations, as obtained by combining the five ICs with their weights and site-specific spatial response, and the time series of the displacements associated with each IC for all GPS stations. The dark gray lines in Figure 4 show the annual + semiannual model, commonly used in GPS time series modeling (Dong et al., 2002), obtained by least squares fit of the GPS observations using the QOCA analyze_tseri package (https://qoca.jpl.nasa.gov). The observed and modeled time series for all GPS stations are provided as supporting information data set.

The temporal evolution of IC2 is indeed similar to the displacement time series measured at CANV station, where the high peak-to-peak displacements observed at CANV (e.g., between 2011 and 2012) have been associated with rainfall-induced southward slope movements of the Alpago-Cansiglio karst plateau (CA in Figure 1) by Devoti et al. (2015). The presence of a similar signal over a much wider region points toward a common physical source, suggesting that rather than being a local feature, ground deformation induced by precipitation is active at a much larger scale. In order to strengthen this hypothesis, we run the ICA analysis excluding CANV. Figure S3 shows the temporal evolution and spatial response associated with IC2 as obtained not excluding CANV. We found no differences both in terms of temporal evolution and spatial

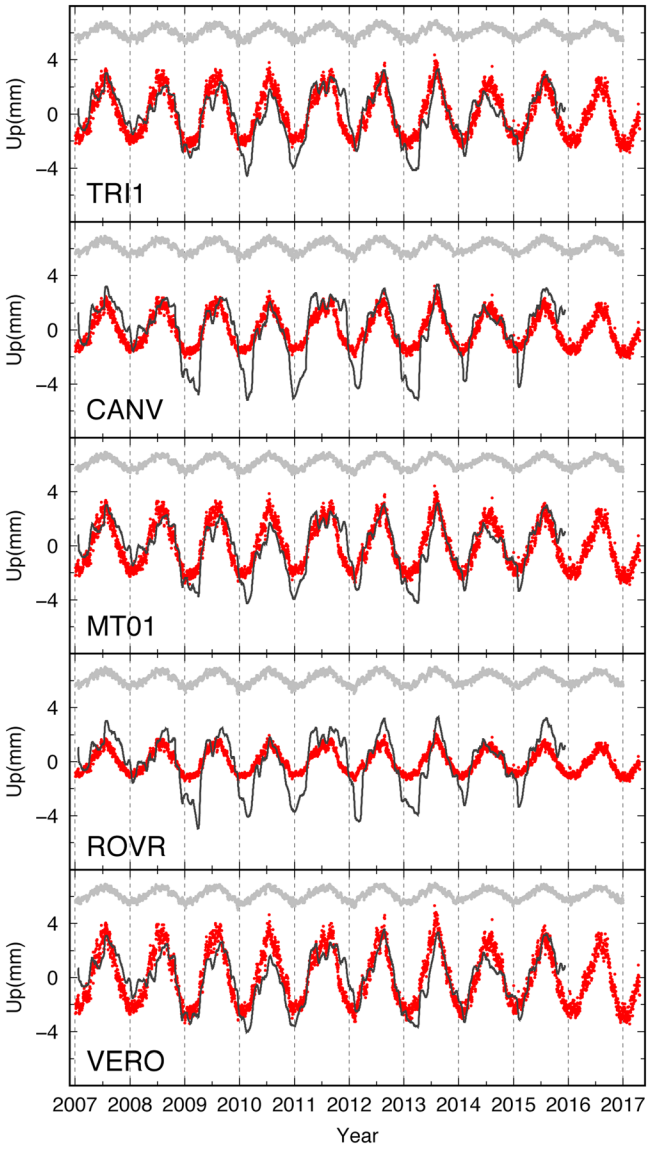

Figure 5. Vertical displacements associated with IC1 (in red) and corresponding surface hydrological loading displacements (black lines) estimated from the ERA-interim (European Centre for Medium-Range Weather Forecasts, ECMWF reanalysis) model (see section 4.2) for a few stations in the study region. In gray the normalized temperature variations at each station from the E-OBS (Haylock et al., 2008) daily gridded observational data set.

response of the ICs, with ICs ordered in terms of weight as in the analysis including CANV. For this reason, in the following we use the results obtained including CANV in the vbICA analysis.

4.2. Seasonal Common Mode Signals

Seasonal displacements, mainly in the vertical components, are well known and described in the literature (e.g., Davis et al., 2012; Dong et al., 2002). Most of seasonal motions can be attributed to loading effects caused by Earth surface and subsurface mass redistributions (e.g., Amos et al., 2014; Argus et al., 2014; Borsa et al., 2014; Tregoning & van Dam, 2005; van Dam et al., 1994). In the study region IC1 and IC3 represent common mode annual signals, displaying rather uniform spatial responses (i.e., with sites moving coherently along the same direction) in the vertical and in the horizontal components, respectively (Figure 3). IC1 describes the larger vertical seasonal displacements (see Figure S4 in the supporting information), with average (median) amplitude of ~3.5 mm and maximum values up to ~10 mm in the vertical component and larger amplitudes at sites located in the pedemountain area. In the horizontal components, IC1 describes much smaller seasonal displacements, with an average (median) amplitude of ~1 mm. In the vertical component, positive peaks, describing uplift of the study region, are in June, and negative peaks, describing subsidence of the area, are in January, being in phase with temperature seasonal variations (see Figure 5). IC3, which is not in phase with temperature, shows positive peaks in spring and negative peaks in autumn, describing annual displacements mainly in the NW-SE directions (see Figure S2), with an average (median) amplitude of ~0.8 and 1.5 mm in the east and north components, respectively.

We compared the displacements associated with IC1 and IC3 with displacements due to the redistribution of fluids at the Earth's surface estimated using recent global reanalysis models. We used predictions provided by http://loading.u-strasbg.fr (Gegout et al., 2010). This service provides global gridded 3-D displacements for atmospheric, hydrological, and nontidal ocean loading obtained from different global models. Surface displacements are computed using Green's function formalism (Farrell, 1972) based on the preliminary reference Earth model assuming a spherically symmetric, nonrotating, elastic, and isotropic Earth (Dziewonski & Anderson, 1981). Daily 3-D surface displacements are provided in the center of figure reference frame with a spatial resolution of 0.5° in longitude and latitude. We used hydrological loading displacement values estimated from ERA-interim (European Centre for Medium-Range Weather Forecasts, ECMWF reanalysis) model (Berrisford et al., 2009; Dee et al., 2011) and from the Global Land Data Assimilation System (GLDAS)/Noah (Rodell et al., 2004) model, for which global grids are provided.

In order to evaluate the agreement between model and geodetic (in terms of ICs) displacements, we use the Lin concordance correlation coefficient (Lin, 1989, 2000), which takes into account similarities on both amplitudes and shapes of two time series. Figures S4 and S5 in the supporting information show maps of the Lin's correlation coefficient values calculated comparing the displacements associated with IC1 and IC3 in the east, north, and vertical components, with hydrological loading displacement values estimated from the ERA-interim and GLDAS models, respectively. The Lin concordance correlation coefficient varies between −1 and 1, with values of 1 denoting perfect concordance and −1 discordance, and a value of 0 denotes its complete absence. The vertical seasonal displacements associated with IC1 are in good agreement with GLDAS and ERA-interim reanalysis hydrological loading models, both in terms of phase and amplitude, whereas the agreement in the horizontal components is poorer. Figure 5 shows the vertical hydrological loading

displacements calculated from the ERA-interim model and the vertical displacements associated with IC1 for a few sites of the study region that are also influenced by the IC2 hydrological signal (see Figure 3).

As regards IC3, both ERA-interim and GLDAS modeled displacements show a better agreement in the north component than the east one (Figures S5 and S6). The displacements obtained by summing IC1 and IC3 show a slight improvement of the agreement with the modeled displacements (see Figures S5 and S6), suggesting anyway that also horizontal seasonal displacements are associated with surface hydrological loading. While it has been well established by Farrell (1972) that assuming a spherical and layered model is the correct way to model both horizontal and vertical components simultaneously, Chanard et al. (2018), modeling Gravity Recovery and Climate Experiment observations, showed that the fit to the phase and amplitude of both horizontal and vertical data can be improved by estimating a degree-1 deformation field rather than using the degree-1 coefficients from Swenson et al. (2008). Regional misfits may also arise from lateral variations of the Earth's elastic parameters, although to a lesser extent than proposed by Chanard et al. (2014) once degree-1 contribution has been adjusted. It is worth considering that other systematic errors in GPS time series can contribute to the annual signals, as shown by Dong et al. (2002), but they marginally contribute to the observed displacements.

4.3. Time-Variable Ground Deformation Associated With IC2

Figure 6 shows the spatial response of IC2 only at sites having a SNR >1. Comparing Figure 6 and Figure 3, it is clear that vertical components associated with IC2 are above the noise level only at a few sites, and for this reason here we focus on the horizontal deformation signal. For IC2 the largest horizontal spatial responses are found at GPS sites located in three sectors of the study region: the Lessini Mountains (area 1 in Figure 6), the Venetian sector of the ESA fold-and-thrust belt, across the Monte Grappa Anticline, (area 2 of Figure 6) and the northern Dinarides (area 3 of Figure 6), across part of the Classical Karst. It is worth considering that being U and S time independent, if V increases (or decreases) between two epochs, the total displacement at a given GPS station between these two epochs will be in the same (or opposite) direction with respect to the green arrows (U vectors) in Figure 6. For example, focusing on the area 2, if we consider the two time intervals where V2 shows large variations, from mid-September to end of December 2010 and from January 2011 to end of April 2012 (T1 and T2 shown in gray tones in Figure 2), in Figure 6 the stations pointing toward SE move southeastward during T1 and then, on average during T2, toward NW (e.g., stations CANV, TAMB, VITT, MGRD, VALX, and MT03), whereas the stations pointing toward NW move northwestward during T1 and then, on average during T2, toward SE (e.g., stations MAVE, FELT, BRSE, BL01, and BLNO). For the T1, T3, T2 and T4 time intervals the cumulative horizontal displacements of GPS sites in area 2 are shown in Figures 7a and 7b, respectively. Excluding CANV, the largest displacements are of the order of ~8 mm. The uncertainties on the cumulative displacement are calculated as the square root of the squared sum of the uncertainties at the two epochs T1 and T2, consistent with the idea that the uncertainties at two different epochs are independent and thus uncorrelated.

A similar behavior, with sites moving alternatively in the opposite directions, is found in the Lessini Mountains (area 1) and in the northern Dinarides (area 3), resulting in a sequence of contractional and extensional deformation associated with the IC2 signal in the three areas. We estimated the temporal evolution of the horizontal strain associated with IC2 using the *analyze_strain* program of the QOCA software (http://qoca.jpl.nasa.gov) applied to the displacement time series associated with IC2 (green lines in Figure 4) for three polygonal areas shown with red lines in Figure 6. The red arrows in Figure 6 show the principal strain directions computed in the three areas with arrows length referring to 2011.0, when strain values are the largest. It is worth considering that the strain axes associated with this signal are oriented consistently with strain rate axes estimated from GPS velocities for long-term tectonic deformation (Figure 5 of Serpelloni et al., 2016).

We analyzed the 90-m resolution Shuttle Radar Topography Mission (http://www2.jpl.nasa.gov/srtm) digital elevation model to characterize the length and orientation of lineaments from topography using the TECLINES software (Rahnama & Gloaguen, 2014a, 2014b). The rose diagrams in Figure 6 show the preferred orientations of these lineaments in the three areas where the spatial response of IC2 is high (dashed boxes in Figure 6). In area 3 lineaments are oriented parallel to the main Dinaric faults, a major active right-lateral strike-slip fault system (Serpelloni et al., 2016). In area 2 lineaments are mainly oriented parallel to the mountain front, where a SW-NE striking active fold-and-thrust-belt is present (Serpelloni et al., 2016). In area 1 there are two different groups of lineaments: one, NW-SE oriented, parallel to Schio-Vicenza fault (see Figure 1) and

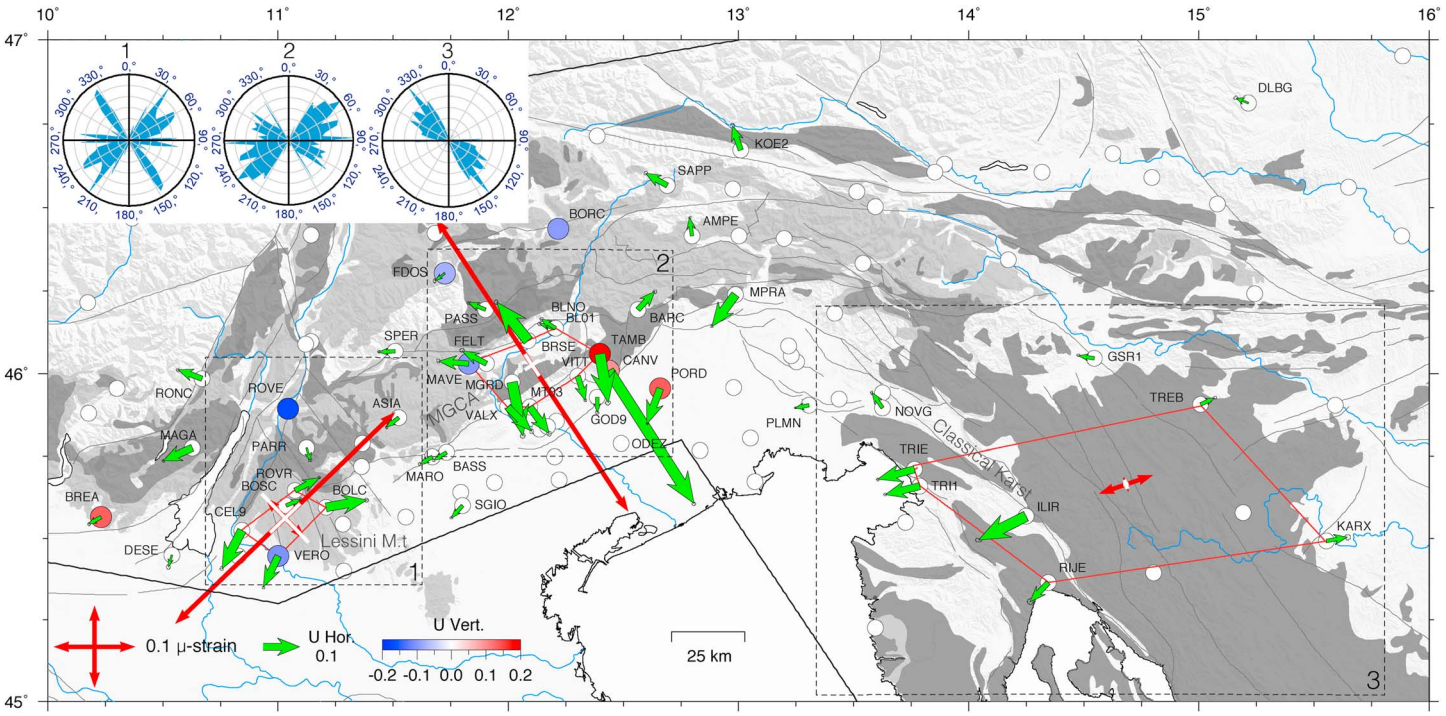

Figure 6. Spatial response (*U*) of IC2 for the vertical (colored circles) and the horizontal (green arrows) components, respectively, as in Figure 3. Here only stations having a SNR > 1 in one of the horizontal component or in the vertical are plotted. The position of other sites (with SNR < 1 for IC2 in all the three components) is plotted as white circles. The red arrows show the principal horizontal strain axes when the highest value of dilatation strain is attained during T1, see Figure 7. Strains are computed using Global Positioning System stations within the associated red polygons. The blue lines show major rivers. The top left inset displays the rose diagrams showing the angular distribution of lineament orientations for the areas delimited by the dashed black boxes (1, 2, and 3), which include sites displaying the largest horizontal spatial response for IC2. The dark and light gray areas represent "highly productive fissured karst aquifers" and "low and moderately productive fissured karst aquifers" from the International Hydrogeological Map of Europe 1:1,500,000 (http://www.bgr.bund.de/ihme1500). MGCA = Monte Grappa-Monte Cesen anticline.

the other one, NE-SW oriented, parallel to the ESA front (as in area 2). The principal strain axes associated with IC2 (red arrows in Figure 6) are normal to the preferred orientations of the lineaments from topography in the three areas. In the area 1 the displacements associated with IC2 at the five stations considered describe two directions of deformation acting about normal to the two main lineament orientations, but the NW-SE oriented strain is smaller and with larger uncertainties.

Focusing on area 2, where the density of GPS sites is higher, the time series of the dilatational strain (Figure 7c) displays a sequence of extensional (positive slopes) and contractional (negative slopes) phases occurring across the Monte Grappa-Cesen Anticline (Figure 6). In the computation of the strain time series for area 2 we have excluded CANV, considering that its larger IC2 spatial response and associated displacements are likely amplified by local topographic/geomorphological effects (Devoti et al., 2016). For areas 1 and 3 the time evolution of dilatational strains is the same, but acting along different directions, as shown in Figure 6. Figure 7c shows that there are two peaks of positive dilatational strain values (with values >0.15 μ strain in area 2), at the end of December 2010 and February 2014, reached through rapid, with an average constant positive rate, increase of dilatational strains, followed by a slower decreasing phase, whose average rate magnitude is decaying with time. The minima (around -0.08 microstrain) occur in autumn 2017, spring/summer 2012 and autumn 2015. It is worth considering that the positive dilatation rate calculated during T1, shown in Figure 7c, is 0.69 microstrain/year^{-1}, which is an order of magnitude greater than the rates of tectonic deformation from GPS velocities in this area (in the range of 0.01–0.06 microstrain/year^{-1}; Danesi et al., 2015).

5. Precipitation Data and IC2

In this section we compare the time evolution of the deformation signal associated with IC2 (i.e., V2) with precipitation. We made use of gridded precipitation data, in the form of daily mean values (in mm) for

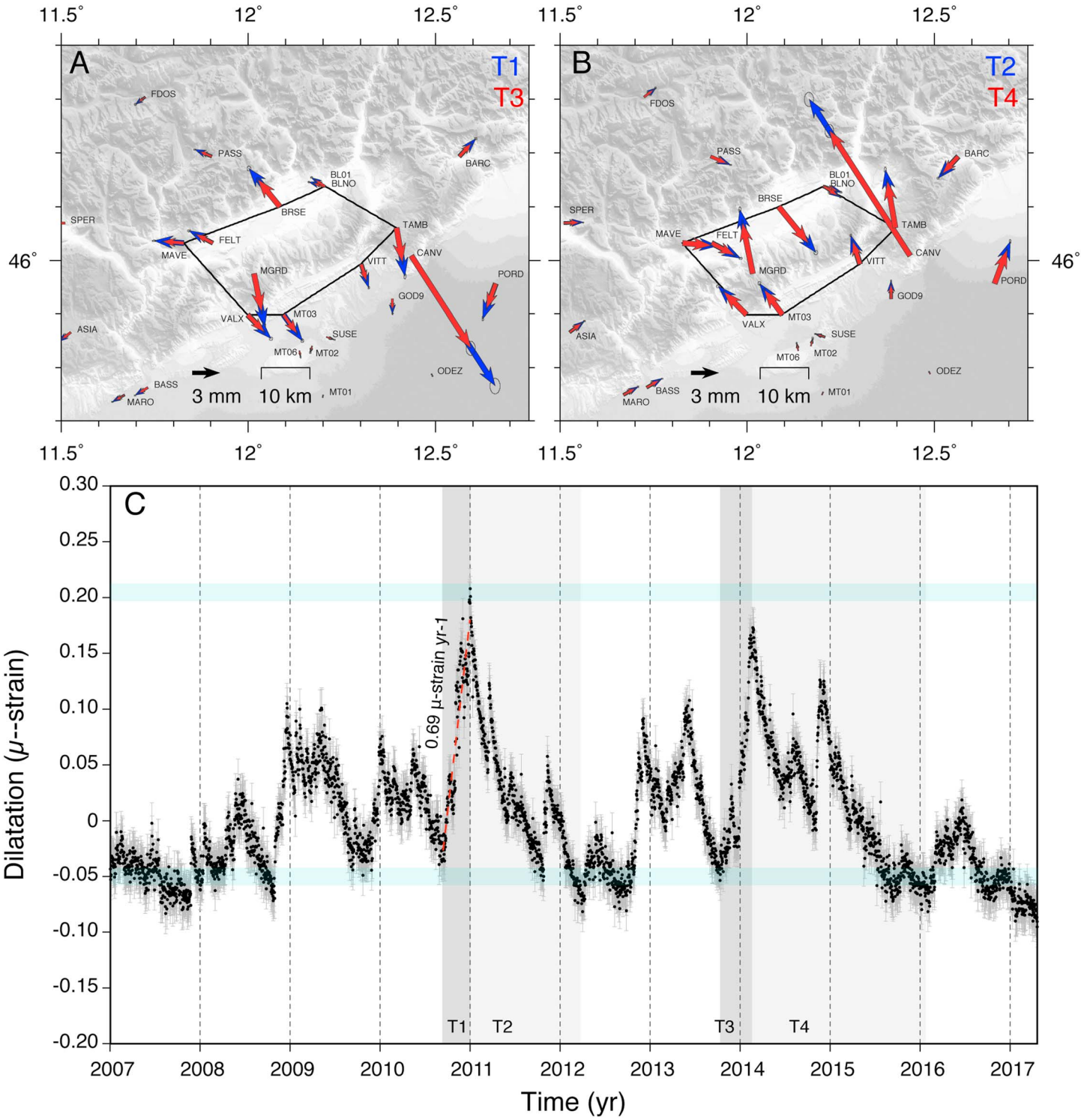

Figure 7. (a, b) Horizontal displacements associated with the IC2 signal in the T1 and T2 (blue arrows) and T3 and T4 (red arrows) time intervals, corresponding to the two periods where larger variations of V2 are present, as discussed in section 4.3. (c) Time series of the dilatational strain (with 1σ uncertainty error bars) obtained from the displacements time series associated with IC2 of stations included in the black polygon shown in (a) and (b). The gray areas indicate the two time intervals (T1 and T2) considered in (a) and (b). The dashed red lines and numbers show the linear fit of the dilatation time series and dilatation rates estimated in T1.

$0.25° \times 0.25°$ resolution cells, obtained from the National Aeronautics and Space Administration precipitation measurement missions (https://pmm.nasa.gov), consisting on satellites carrying advanced radar/radiometer systems to measure global precipitation from space. In particular, we used data from the Tropical Rainfall

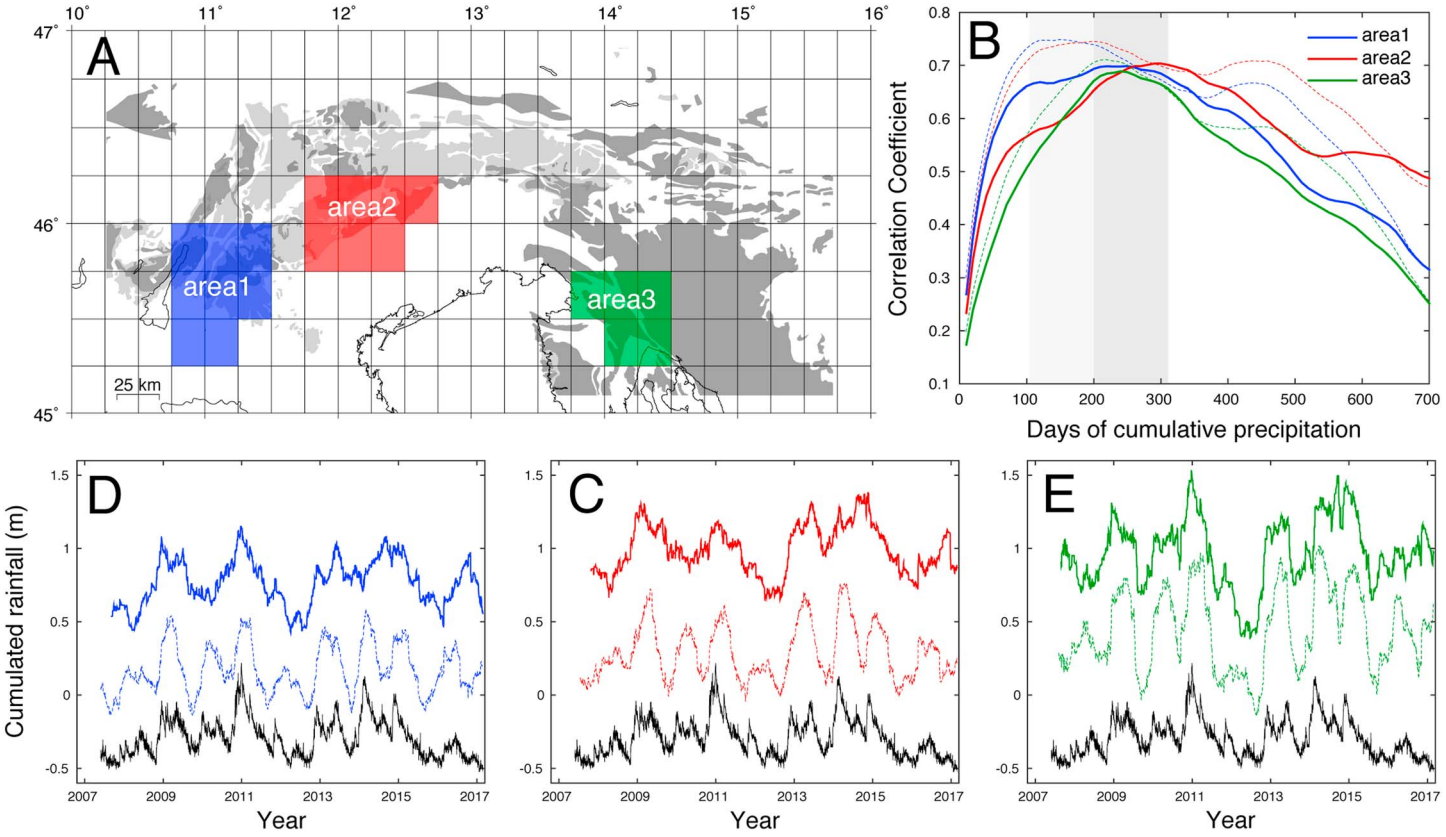

Figure 8. (a) The 0.25° × 0.25° grid of the Tropical Rainfall Measuring Mission-Global Precipitation Measurements precipitation data, where the blue, red, and green regions are the sectors used to compute the curves of cumulative precipitation for the three areas in (b). (b) Correlation coefficient between V2 and the curves of cumulated precipitation as a function of the number of days used to calculate cumulative precipitation values for the three areas shown in (a), as described in section 5. Solid and dashed lines refer to curves obtained using precipitation, P, and P-ET, respectively. (c–e) V2 (in black) and the curves of cumulative precipitation obtained using the number of days providing the maximum value of the correlation coefficient for the three areas in (a) using precipitation, P (solid lines), and P-ET (dashed lines).

Measuring Mission, integrated for 2017 by data from the Global Precipitation Measurements (GPMsatellite mission (Goddard Earth Sciences Data and Information Services Center (2016). In the supporting information (Texts S1 and S2) we provide a comparison between the precipitation curves obtained from satellite measurements, local pluviometric stations and other gridded data sets from meteoclimatic models using data from European pluviometric networks (Haylock et al., 2008).

We focus the analysis on the three areas where the spatial response of IC2 is larger, using the grid cells shown in Figure 8a. We perform this analysis using both the original precipitation values (P) and the precipitation corrected for the potential evapotranspiration (ET) component, P-ET. It is important to emphasize that real ET is difficult to measure or estimate (Villagra et al., 1995), since it depends on different controlling factors, among which the most important ones are temperature and humidity of the air, water condition of the soil, and land use and pedological characteristic of the catchment. Moreover, it is worth considering that the high permeability of rocks outcropping in karst regions favors a rapid infiltration; thus, models of ET applied in these areas may be inaccurate. To evaluate the influence of ET, we used daily ET values calculated from the ECMWF meteorological model (Dee et al., 2011), which are provided with the same temporal and spatial resolution of the gridded precipitation data.

We found no correlation between V2 and the daily precipitation. The correlation between V2 and the cumulative (for the 2007–2017 time span considered) and de-trended precipitation curve for the three areas is also low (see Figure S11 and Table 1). Computing the cross correlation, we found a slight improvement of the correlation (Table 1), with the precipitation curve anticipating V2 of 9 to 30 days. Considering P-ET slightly improves both the correlation and cross-correlation values with V2, with correlation coefficients between 0.3 and 0.5. We then compared V2 with curves of cumulated precipitation over different time windows. In

Table 1
Results of the Correlation and Cross-Correlation Analyses Between V2 and Precipitation

Area	CUM_DET	PET_CUM_DET	CUM_DET CC	TL (days)	PET_CUM_DET CC	TL_E (days)	CUM_VW	N. Days	PET_CUM_VW	N. days
1	0.2677	0.3732	0.2924	31	0.4051	25	0.6985	250	0.8493	150
2	0.4143	0.5023	0.416	9	0.5134	14	0.7034	300	0.746	200
3	0.2592	0.3252	0.2631	9	0.3338	11	0.6888	240	0.7111	220

Note. P. CUM_DET: correlation coefficient between V2 and de-trended cumulative precipitation (estimated over the entire 2007–2017 time span); PET_CUM_DET: correlation coefficient between V2 and de-trended cumulative P-ET (estimated over the entire time span); CUM_DET_CC: cross correlation between V2 and de-trended cumulative P-ET: TL: time lag between V2 and de-trended cumulative P-ET curve (where CUM_DET_CC anticipate V2); PET_CUM_DET: correlation coefficient between V2 and de-trended cumulative P-ET (estimated over the entire time span); TL_E: time lag between V2 and de-trended cumulative P-ET curve (where PET_CUM_DET_CC anticipate V2); CUM_VW: correlation coefficient between V2 and the cumulated precipitation curve obtained by using the number of days (N. Days) that maximize the correlation; PET_CUM_VW: same as CUM_VW except that P-ET is used.

particular, for each area we computed cumulated precipitation curves by summing, and for each day, the precipitation occurred during a certain number of days before. The correlation coefficient between V2 and the curve of cumulative precipitation depends on the number of days of cumulated precipitation (solid lines in Figure 8b), with the highest correlation (~0.7) found using 250, 300, and 240 days for areas 1, 2, and 3, respectively. Panels (c)–(e) in Figure 8 compare the corresponding cumulative precipitation curves (solid lines) with V2. Using P-ET provides an improvement of the correlation coefficient, which is maximized using 150, 200, and 220 days of cumulated P-ET values (see Table 1).

6. Interpreting the Link Between Precipitation and Deformation

The correlation between V2 and cumulated precipitation curves points toward a common hydrological forcing for the observed time-variable deformation signal in the ESA and northern Dinarides. The orientation of the horizontal strain axes associated with IC2 (Figure 6) suggests that this hydrological forcing acts on existing rock fractures and the signal is amplified in karst terrains. At a local scale, water infiltration and associated pressure change was proposed to explain tilt and surface deformation signals in fractured outcrops (e.g., Devoti et al., 2015; Jacob et al., 2010; Longuevergne et al., 2009; Schuite et al., 2015). Important water level changes (of the order of tens of meters) are common in karst environments (Milanović, 2005, 2014), where narrow fractures can drain water from large areas, focusing the effects of pressure changes within thin, subvertical structures. Water level rise and subsequent draining could therefore account for the observed alternating phases of extension and contraction across fractures. The time windows that maximize the correlation between V2 and cumulated precipitation curves (Figure 8) might relate to the time needed to saturate and then drain these structures and depends on the different rates at which groundwater can flow in a karstic environment. According to Maillet (1905), the emptying of a reservoir through a porous outlet is described by $Q_t = Q_0 \exp(-\alpha t)$, where Q_t is the discharge at time t, Q_0 is the discharge at the start of the recession, and α (in d^{-1}) is a recession coefficient that depends upon the geological and morphological structure of the catchment. This equation has been widely used to describe the discharge hydrographs of karst aquifers to constrain their transportation and storage characteristics. Recession coefficients evaluated for karst springs systems in France and Jordan Valley are in the range of $0.004 \div 0.006\ d^{-1}$ (e.g., Fleury et al., 2007; Forkasiewicz & Paloc, 1967; Milanović, 1981; Sauter, 1992; Schmidt et al., 2014). These values indicate that the time scale of the diffusion time of the water within a karst aquifer is generally about 160 ÷ 250 days, which is consistent with our results.

Opening/recharge phases reflect faster water flows associated with positive linear trends of dilatational strain (e.g., T1 in Figure 7c), while the closing/discharge phases relates to slower and nonlinear negative trends (e.g., part of T2 in Figure 7c). This different behavior resembles that of typical unit hydrographs or karst spring hydrographs (Milanović, 1981). This could be explained by different dominant flow regimes characterizing the hydraulic responses during the recharge and discharge phases, as also proposed by Devoti et al. (2015) for the Cansiglio Plateau.

The spatial extent of the detected hydrogeodetic deformation suggests that this is likely the cumulated result of several distinct sources within the fractured karst system; together, these sources form a geodetic signal whose wavelength is longer than that of signals recorded at a local scale, using tiltmeters installed in natural caves (e.g., Grillo et al., 2011). The contribution of each distinct deformation source is practically impossible to

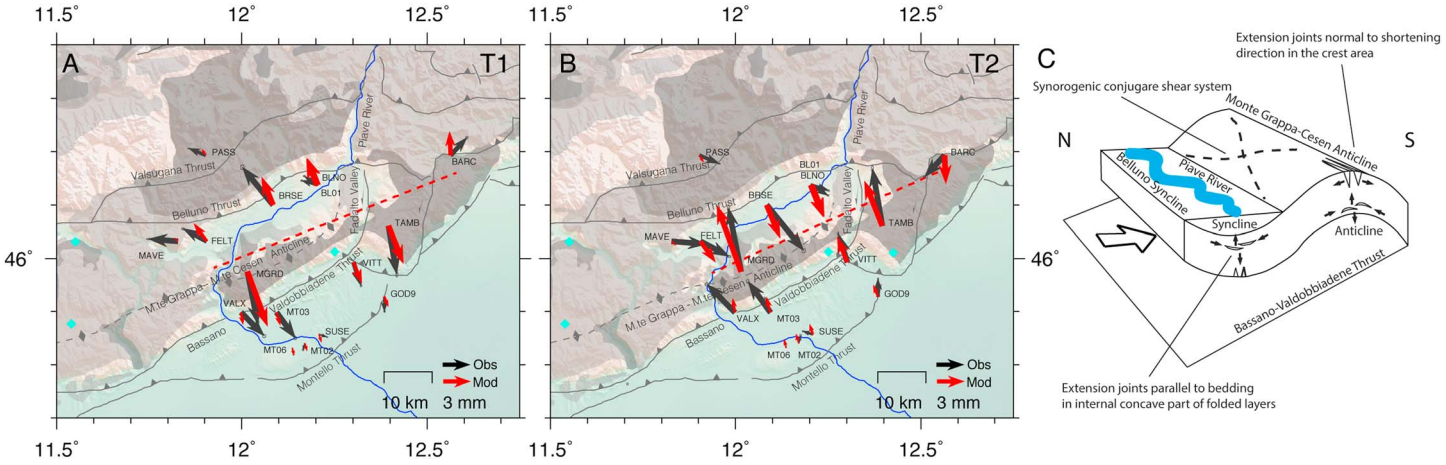

Figure 9. (a and b) Observed (black) and modeled (red) horizontal displacements during the T1 and T2 time intervals (see also Figure 7), respectively, using an effective vertical tensile dislocation (dashed red line), as discussed in section 6. The blue line is the Piave River and the cyan diamonds show locations of major karst springs (Cavallo et al., 2003). The dark and light gray areas represent highly productive fissured karst aquifers and low and moderately productive fissured karst aquifer from the International Hydrogeological Map of Europe 1:1,500,000 (http://www.bgr.bund.de/ihme1500). (c) Simplified sketch of the geological structure of the Belluno syncline and the Monte Grappa-Monte Cesen Anticline, with fold terminology from Ramsay and Huber (1983).

estimate because of the numerous parameters involved, including fractures number, density, dimension, position, orientation, and opening/closing values. However, we can approximate their overall behavior as the one due to a single, equivalent tensile fracture (e.g., Jade & Sitharam, 2003; Sitharam et al., 2001), to gain a first-order estimation of the pressure changes required to explain the observed horizontal displacement patterns. A similar approach has been used by Silverii et al. (2016) to model displacements associated with karst aquifers in the southern Apennines with elastic dislocation.

We focus on area 2 (Figure 6), where the GPS network is denser than areas 1 and 3, thanks to past geodetic experiments (Danesi et al., 2015) and used only horizontal displacements. We have excluded the site CANV, since the larger displacements observed at this site may also result from topographic amplification of the rainfall-induced deformation signal (Guglielmi et al., 2005), being this station located at the edge of the steep slope of the Cansiglio plateau (see also Devoti et al., 2016). In area 2 the horizontal principal strain axes associated with IC2 are normal to the seismically active pedemountain front and parallel to the direction of the long-term tectonic and geological deformation (see Figure 5 in Serpelloni et al., 2016). For this reason, the deformation associated with this hydrological signal could be potentially misinterpreted with a transient of tectonic origin, for example, if analyzed only across limited time intervals. Moreover, some of the stations largely affected by the hydrological deformation, coincides with stations that poorly fit elastic interseismic models (see Figure 10 of Serpelloni et al., 2016), posing the problem of how these stations can be used for tectonic studies.

Considering the two time intervals T1 (mid-September to December 2010) and T2 (January 2011 to April 2012), corresponding to extensional and compressional phases (Figure 7c), we can describe the displacements associated with IC2 (black arrows in Figures 7a and 7b) as due to a variable opening of a tensile dislocation (i.e., the equivalent tensile fracture). The observed ground displacements are best reproduced considering a rectangular, vertical tensile dislocation in an elastic half-space (Poisson's ratio of 0.25) whose orientation is consistent with orientation of lineaments from topography (Figure 6 and Text S3 in the supporting information; Cervelli et al., 2001; Okada, 1985), while fixing its center position. While length and strike are rather well constrained, the depth (1.1 km) is affected by a greater uncertainty (Figure S12), indicating anyhow that the deformation wavelength of the signal is likely associated with a structure as deep as 1 km. This is in agreement with the presence of a deep-rooted karst system in this area (Mietto & Sauro, 2000). Structurally, this area corresponds to a NE-SW oriented syncline-anticline pair confined between two regional thrusts, the Bassano-Valdobbiadene thrust, and the Valsugana thrust (see Figure 9c). The idealized equivalent tensile fracture might correspond with subvertical synfolding fractures originated in the hinge zone of the Monte Grappa-Monte Cesen-Col Visentin Anticline, where a "highly productive" karst aquifer (following the notation of the International Hydrogeological Map of Europe) is present along the anticline structure

(Figure 9). We can speculate that this system of fold-related subvertical fractures represents relatively narrow structural features that may drain water from large areas and react to the related pressure changes, causing the observed anisotropic displacements at the GPS stations.

Assuming a rigidity modulus of 30×10^9 Pa and a uniform pressure change along the tensile fracture surface, with a geometry defined by the mean parameter values (red dashed line in Figure 9), the horizontal displacements can be modeled through a boundary elements approach (Ferrari et al., 2016). For the T1 and T2 intervals, a pressure increment of 790 kPa in ~110 days and drop of 950 kPa in ~450 days, respectively, minimizes the misfit between modeled (red arrows in Figure 9) and measured horizontal displacements. Similar root-mean-square misfit values of 2.1 and 2.6 mm are obtained by uniform opening of 4.3 cm and closing of 5.2 cm in the tensile dislocation model as well, capturing the first-order features of the original displacements. The pressure changes associated with opening and closing of the vertical tensile dislocation in area 2 correspond to a water level increase of ~80 m during the opening phase (T1) and a water level drop of ~97 m during the closure phase (T2). Groundwater fluctuations of the same order of magnitude (tens to hundreds of meters) over time spans like T1 and T2 (months) are common in high-developed karsts (Milanović, 2005, 2014). Similar values of positive pressure changes (i.e., water level rise) can be expected for a second period of larger positive variations of V2, which is between November 2013 and February 2014 (T3 in Figure 7), after which there is a general negative trend of the dilatational strain lasting to 2017, with two smaller phases of positive trends in the winter 2015 and summer 2016.

We can speculate that the same mechanism is active in the Lessini Mountains (area 1) and the Classical Karst (area 3), where subvertical strike-slip faults, oriented normal to the observed hydrogeodetic strain axes, are well developed and deep-rooted karst aquifers are present. In these two areas, however, additional cGPS sites would be necessary to better characterize the kinematic pattern of this deformation signal. Similarly, additional cGPS stations would be necessary to better describe the spatial extent of the hydrogeodetic signal around the Cansiglio Plateau, which would also help discriminating eventual different sources of deformation associated with the Monte Grappa-Cesen Anticline and the Cansiglio Plateau regions.

7. Conclusions

GPS ground displacements in the ESA and northern Dinarides are driven by hydrological processes acting at different spatial scales and with different temporal evolution. Changes of surface hydrological loads are responsible for the observed seasonal common mode displacements, which are significantly larger in the vertical components showing the whole region moving up and down with an annual period. On the contrary, we found new evidence of rainfall-induced horizontal deformation with amplitudes and orientations controlled by structural and geological features in karst terrains. In three different karstic areas of the study region we observe stations moving in the opposite directions and reversing the sense of movement in time, implying a succession of extensional/compressional strains with variable amplitudes through time, acting normal to rock fractures. The evolution of ground displacements and dilatational strains associated with this signal correlate with cumulated precipitation curves obtained by summing, for each day, the precipitation occurred during a certain number of days before, with the number of days maximizing the correlation varying between 150–220 and 240–300 days, if P-ET is used or not, respectively.

We propose that the observed alternating phases of dilation and contraction are modulated by the hydrogeological cycle, where the balance between meteoric recharge (precipitation and infiltration from a wide area) and water discharge determine the elevation of the water table within fractures, controlling the distribution of hydrostatic pressure and its temporal fluctuations. Focusing on the sector where the GPS network allows for a better sampling of this hydrogeodetic deformation signal, which is the Monte Grappa-Cesen Anticline, we found that pressure increment of 790 KPa in ~110 days and pressure drop of 950 KPa in ~450 days, in an equivalent tensile fracture extending down to ~1 km from the surface, are required to reproduce the first-order features of the displacement field during the two periods of larger variations of the strain values.

We have shown that optimal source separation in GPS displacement time series is a fundamental task in order to accurately measure small (millimeter-level) nonseasonal or transient deformation signals, such as the ones associated with precipitation and groundwater flow. The impact of rainfall-induced deformation processes on the tectonic deformation needs to be reconsidered. Possible implications regard the length of the GPS time series required for an accurate estimate of the linear tectonic trends and the influence of this time-

variable deformation on the stress state at depths, and eventually on the seismicity rates. Karst systems confirmed to be peculiar geological features where space geodesy may significantly contribute in monitoring groundwater resources. Future works will include the inclusion of additional GPS stations and the development of hydrological and numerical models.

Acknowledgments

The authors thank the Editor, Paul Tregoning, Eric Calais, and Philippe Vernant for the constructive comments that improved the impact and readability of this manuscript. We thank Jo De Waele, Paolo Forti, and Marco Antonellini (University of Bologna) and Dario Zampieri (University of Padova) for the useful discussions at an early stage of this work. We thank Mehdi Rahnama for his support in the use of the TecLines software. We thank Jean-Paul Boy (Institut de Physique du Globe de Strasbourg) for providing the time series of the displacements caused by atmospheric, oceanic, and hydrological loading at the GPS stations coordinates. We are grateful to all public and private institutions that made the continuous GPS data used in this work freely available and, in particular, INGV and OGS personnel for maintaining the RING (DOI:10.13127/RING) and FredNet (http://frednet.crs.inogs.it) networks and ARPAV Belluno for providing us with data of MAVE and BOSC stations. The TRMM daily precipitation data are available from the NASA Goddard Earth Sciences Data and Information Services Center (GES DISC): https://disc.gsfc.nasa.gov/datacollection/TRMM_3B42_Daily_7.html. The daily evapotranspiration data are available from the European Centre for Medium-Range Weather Forecasts (ECMWF) at the following link: http://apps.ecmwf.int/datasets/data/interim-full-daily. We acknowledge the E-OBS data set from the EU-FP6 project ENSEMBLES (http://ensembles-eu.metoffice.com) and the data providers in the ECA&D project (http://www.ecad.eu). The de-trended GPS time series data used as input of the vbICA analysis are available as supporting information Data Set S1. The raw GPS data not available through freely accessible archives can be obtained by contacting the first author (enrico.serpelloni@ingv.it). Most of the figures were made using the GMT software (Wessel et al., 2013). This work has been developed in the framework of the project TRANSIENTI, founded by the Italian Ministry of Education, Universities and Research (MIUR) "Premiale 2014."

References

Altamimi, Z., Collilieux, X., & Métivier, L. (2011). ITRF2008: An improved solution of the international terrestrial reference frame. *Journal of Geodesy*, *85*(8), 457–473. https://doi.org/10.1007/s00190-011-0444-4

Amiri-Simkooei, A. R., Mohammadloo, T. H., & Argus, D. F. (2017). Multivariate analysis of GPS position time series of JPL second reprocessing campaign. *Journal of Geodesy*, *91*(6), 685–704. https://doi.org/10.1007/s00190-016-0991-9

Amoruso, A., Crescentini, L., & Chiaraluce, L. (2017). Surface temperature and precipitation affecting GPS signals before the 2009 L'Aquila earthquake (Central Italy). *Geophysical Journal International*, *210*(2), 911–918. https://doi.org/10.1093/gji/ggx210

Amos, C. B., Audet, P., Hammond, W. C., Bürgmann, R., Johanson, I. A., & Blewitt, G. (2014). Uplift and seismicity driven by groundwater depletion in central California. *Nature*, *509*(7501), 483–486. https://doi.org/10.1038/nature13275

Argus, D. F., Fu, Y., & Landerer, F. W. (2014). Seasonal variation in total waterstorage in California inferred from GPSobservations of vertical land motion. *Geophysical Research Letters*, *41*, 1971–1980. https://doi.org/10.1002/2014GL059570

Berrisford, P., Dee, D., Fielding, K., Fuentes, M., Kallberg, P., Kobayashi, S., & Uppala, S. (2009). *The ERA-Interim archive*, *ERA Rep. Ser.* (Vol. 1). Reading, UK: Eur. Cent. for Medium Range Forecasts.

Bettinelli, P., Avouac, J.-P., Flouzat, M., Bollinger, L., Ramillien, G., Rajaure, S., & Sapkota, S. (2008). Seasonal variations of seismicity and geodetic strain in the Himalaya induced by surface hydrology. *Earth and Planetary Science Letters*, *266*(3–4), 332–344. https://doi.org/10.1016/j.epsl.2007.11.021

Blewitt, G., & Lavallee, D. (2002). Effect of annual signals on geodetic velocity. *Journal of Geophysical Research*, *107*(B7), 2145. https://doi.org/10.1029/2001JB000570

Boehm, J., Werl, B., & Schuh, H. (2006). Troposphere mapping functions for GPS and very long baseline interferometry from European Centre for Medium-Range Weather Forecasts operational analysis data. *Journal of Geophysical Research*, *111*, B02406. https://doi.org/10.1029/2005JB003629

Boergens, E., Rangelova, E., Sideris, M. G., & Kusche, J. (2014). Assessment of the capabilities of the temporal and spatiotemporal ICA method for geophysical signal separation in GRACE data. *Journal of Geophysical Research: Solid Earth*, *119*, 4429–4447. https://doi.org/10.1002/2013JB010452

Borsa, A. A., Agnew, D. C., & Cayan, D. R. (2014). Ongoing drought-induced uplift in the western United States. *Science*, *345*(6204), 1587–1590. https://doi.org/10.1126/science.1260279

Cavallo, C., Dal Molin, L., De Waele, J., Mietto, P., Piccini, L., Preziosi, E., et al. (2003). Il censimento delle sorgenti carsiche d'Italia, Atti del XIX Congresso Nazionale di Speleologia (Vol. 2, pp. 29–34). Bologna, 27–31 Agosto, 2003.

Cervelli, P., Murray, M. H., Segall, P., Aoki, Y., & Kato, T. (2001). Estimating source parameters from deformation data, with an application to the March 1997 earthquake swarm off the Izu Peninsula, Japan. *Journal of Geophysical Research*, *106*(B6), 11,217–11,237. https://doi.org/10.1029/2000JB900399

Chan, K. L., Lee, T. W., & Sejnowski, T. J. (2003). Variational Bayesian learning of ICA with missing data. *Neural Computation*, *15*(8), 1991–2011. https://doi.org/10.1162/08997660360675116

Chanard, K., Avouac, J. P., Ramillien, G., & Genrich, J. (2014). Modeling deformation induced by seasonal variations of continental water in the Himalaya region: Sensitivity to Earth elastic structure. *Journal of Geophysical Research: Solid Earth*, *119*, 5097–5113. https://doi.org/10.1002/2013JB010451

Chanard, K., Fleitout, L., Calais, E., Rebischung, P., & Avouac, J. P. (2018). Toward a global horizontal and vertical elastic load deformation model derived from GRACE and GNSS station position time series. *Journal of Geophysical Research: Solid Earth*, *128*. https://doi.org/10.1002/2017JB015245

Cheloni, D., D'Agostino, N., & Selvaggi, G. (2014). Interseismic coupling, seismic potential, and earthquake recurrence on the southern front of the Eastern Alps (NE Italy). *Journal of Geophysical Research: Solid Earth*, *119*, 4448–4468. https://doi.org/10.1002/2014JB010954

Choudrey, R. A., & Roberts, S. J. (2003). Variational mixture of Bayesian independent component analyzers. *Neural Computation*, *15*(1), 213–252. https://doi.org/10.1162/089976603321043766

Dal Moro, G., & Zadro, M. (1998). Subsurface deformations induced by rainfall and atmospheric pressure: Tilt/strain measurements in the NE-Italy seismic area. *Earth and Planetary Science Letters*, *164*(1–2), 193–203. https://doi.org/10.1016/S0012-821X(98)00203-9

Danesi, S., Pondrelli, S., Salimbeni, S., Cavaliere, A., Serpelloni, E., Danecek, P., et al. (2015). Active deformation and seismicity in the Southern Alps (Italy): The Montello hill as a case study. *Tectonophysics*, *653*, 95–108. https://doi.org/10.1016/j.tecto.2015.03.028

Davis, J. L., Wernicke, B. P., & Tamisiea, M. E. (2012). On seasonal signals in geodetic time series. *Journal of Geophysical Research*, *117*, B01403. https://doi.org/10.1029/2011JB008690

Decker, K., & Peresson, H. (1996). Tertiary kinematics in the Alpine-Carpathian-Pannonian system: Links between thrusting, transform faulting and crustal extension. In G. Wessely & W. Liebl (Eds.), *Oil and gas in alpidic thrust belts and basins of central and eastern Europe*, *EAGE Spec. Publ* (Vol. 5, pp. 69–77). London: The Geological Society.

Dee, D., Uppala, S., Simmons, A., Berrisford, P., Poli, P., Kobayashi, S., et al. (2011). The ERA-Interim reanalysis: Configuration and performance of the data assimilation system. *Quarterly Journal of the Royal Meteorological Society*, *137*(656), 553–597. https://doi.org/10.1002/qj.828

Devoti, R., D'Agostino, N., Serpelloni, E., Pietrantonio, G., Riguzzi, F., Avallone, A., et al. (2017). A combined velocity field of the Mediterranean region. *Annals of Geophysics*, *60*(2), S0215. https://doi.org/10.4401/ag-7059

Devoti, R., Falcucci, E., Gori, S., Poli, M. E., Zanferrari, A., Braitenberg, C., et al. (2016). Karstic slope "breathing": Morpho-structural influence and hazard implications. *Geophysical Research Abstracts*, *18*, EGU2016–EGU15231.

Devoti, R., Zuliani, D., Braitenberg, C., Fabris, P., & Grillo, B. (2015). Hydrologically induced slope deformations detected by GPS and clinometric surveys in the Cansiglio Plateau, Southern Alps. *Earth and Planetary Science Letters*, *419*, 134–142. https://doi.org/10.1016/j.epsl.2015.03.023

Dong, D., Fang, P., Bock, Y., Cheng, M., & Miyazaki, S. (2002). Anatomy of apparent seasonal variations from GPS-derived site position time series. *Journal of Geophysical Research*, *107*(B4), 2075. https://doi.org/10.1029/2001JB000573

Dong, D., Fang, P., Bock, Y., Webb, F., Prawirodirdjo, L., Kedar, S., & Jamason, P. (2006). Spatiotemporal filtering using principal component analysis and Karhunen-Loeve expansion approaches for regional GPS network analysis. *Journal of Geophysical Research*, *111*, B03405. https://doi.org/10.1029/2005JB003806

Dong, D., Herring, T., & King, R. (1998). Estimating regional deformation from a combination of space and terrestrial geodetic data. *Journal of Geodesy*, *72*(4), 200–214. https://doi.org/10.1007/s001900050161

Dziewonski, A. M., & Anderson, D. L. (1981). Preliminary reference Earth model. *Physics of the Earth and Planetary Interiors*, *25*(4), 297–356. https://doi.org/10.1016/0031-9201(81)90046-7

Evans, K., & Wyatt, F. (1984). Water table effects on the measurement of Earth strain. *Tectonophysics*, *108*(3-4), 323–337. https://doi.org/10.1016/0040-1951(84)90242-7

Farrell, W. E. (1972). Deformation of the Earth by surface loads. *Reviews of Geophysics*, *10*(3), 761. https://doi.org/10.1029/RG010i003p00761

Ferrari, C., Bonafede, M., & Belardinelli, M. E. (2016). LibHalfSpace: A C++ object-oriented library to study deformation and stress in elastic half-spaces. *Computers & Geosciences*, *96*, 136–146. https://doi.org/10.1016/j.cageo.2016.08.011

Fleury, P., Plagnes, V., & Bakalowicz, M. (2007). Modelling of the functioning of karst aquifers with a reservoir model: Application to Fontaine de Vaucluse (South of France). *Journal of Hydrology*, *345*(1–2), 38–49. https://doi.org/10.1016/j.jhydrol.2007.07.014

Forkasiewicz, J., & Paloc, H. (1967). Le régime de tarissement de la Foux de la Vis, etude préliminaire. In *Hydrology of fractured rocks proccedings of the Dubrovnik Symposium, October 1965* (Vol. 1, pp. 213–226).

Fu, Y., Argus, D. F., Freymueller, J. T., & Heflin, M. B. (2013). Horizontal motion in elastic response to seasonal loading of rain water in the Amazon Basin and monsoon water in Southeast Asia observed by GPS and inferred from GRACE. *Geophysical Research Letters*, *40*, 6048–6053. https://doi.org/10.1002/2013GL058093

Gegout, P., Boy, J.-P., Hinderer, J., & Ferhat, G. (2010). Modeling and observation of loading contribution to time-variable GPS sites positions. *International Association of Geodesy Symposia*, *135*(8), 651–659. https://doi.org/10.1007/978-3-642-10634-7_86

Gilli, E., Boudin, F., Longuevergne, L., Florsch, N., Walch, J.-J., Gomez, A., et al. (2010). Neotectonics and current hydrologically-induced karst deformation. Case study of the Plateau de Calern (Alpes-Maritimes, France). *Geodinamica Acta*, *23*(1–3), 49–64. https://doi.org/10.3166/ga.23.49-64

Goddard Earth Sciences Data and Information Services Center (2016). TRMM (TMPA) precipitation L3 1 day 0.25 degree × 0.25 degree V7, Goddard Earth Sciences Data and Information Services Center (GES DISC). Retrieved from https://disc.gsfc.nasa.gov/datacollection/TRMM_3B42_Daily_7.html, Accessed (March 2017).

Grillo, B., Braitenberg, C., Devoti, R., & Nagy, I. (2011). The study of karstic aquifers by geodetic measurements in Bus de la Genziana station-Cansiglio plateau (Northeastern Italy). *Acta Carsologica*, *40*(1), 161–173. https://doi.org/10.3986/ac.v40i1.35

Gualandi, A., Avouac, J. P., Galetzka, J., Genrich, J. F., Blewitt, G., Adhikari, L. B., et al. (2016). Pre- and post-seismic deformation related to the 2015, M_w7.8 Gorkha earthquake, Nepal. *Tectonophysics*, *714-715*, 90–106. https://doi.org/10.1016/j.tecto.2016.06.014

Gualandi, A., Nichele, C., Serpelloni, E., Chiaraluce, L., Anderlini, L., Latorre, D., et al. (2017). Aseismic deformation associated with an earthquake swarm in the northern Apennines (Italy). *Geophysical Research Letters*, *44*, 7706–7714. https://doi.org/10.1002/2017GL073687

Gualandi, A., Perfettini, H., Radiguet, M., Cotte, N., & Kostoglodov, V. (2017). GPS deformation related to the M_w7.3, 2014, Papanoa earthquake (Mexico) reveals the aseismic behavior of the Guerrero seismic gap. *Geophysical Research Letters*, *44*, 6039–6047. https://doi.org/10.1002/2017GL072913

Gualandi, A., Serpelloni, E., & Belardinelli, M. E. (2016). Blind source separation problem in GPS time series. *Journal of Geodesy*, *90*(4), 323–341. https://doi.org/10.1007/s00190-015-0875-4

Guglielmi, Y., Cappa, F., & Binet, S. (2005). Coupling between hydrogeology and deformation of mountainous rock slopes: Insights from La Clapière area (Southern Alps, France). *Comptes Rendus Geoscience*, *337*(13), 1154–1163. https://doi.org/10.1016/j.crte.2005.04.016

Hainzl, S., Kraft, T., Wassermann, J., Igel, H., & Schmedes, E. (2006). Evidence for rainfall-triggered earthquake activity. *Geophysical Research Letters*, *33*, L19303. https://doi.org/10.1029/2006GL027642

Haylock, M. R., Hofstra, N., Klein Tank, A. M. G., Klok, E. J., Jones, P. D., & New, M. (2008). A European daily high-resolution gridded data set of surface temperature and precipitation for 1950–2006. *Journal of Geophysical Research*, *113*, D20119. https://doi.org/10.1029/2008JD010201

Herring, T. A., King, R. W., Floyd, M. A., & McClusky, S. C. (2015). Introduction to GAMIT/GLOBK, Release 10.6. Retrieved from http://www-gpsg.mit.edu/~simon/gtgk/Intro_GG.pdf

Jacob, T., Chery, J., Boudin, F., & Bayer, R. (2010). Monitoring deformation from hydrologic processes in a karst aquifer using long-baseline tiltmeters. *Water Resources Research*, *46*, W09542. https://doi.org/10.1029/2009WR008082

Jade, S., & Sitharam, T. (2003). Characterization of strength and deformation of jointed rock mass based on statistical analysis. *International Journal of Geomechanics*, *3*(1), 43–54. https://doi.org/10.1061/(ASCE)1532-3641(2003)3:1(43)

Jahr, T., Jentzsch, G., & Gebauer, A. (2008). Deformation, seismicity, and fluids: Results of the 2004/2005 water injection experiment at the KTB/Germany. *Journal of Geophysical Research*, *113*, B11410. https://doi.org/10.1029/2008JB005610

Ji, K. H., & Herring, T. A. (2012). Correlation between changes in groundwater levels and surface deformation from GPS measurements in the San Gabriel Valley, California. *Geophysical Research Letters*, *39*, L01301. https://doi.org/10.1029/2011GL050195

Jiang, Y., Dixon, T. H., & Wdowinski, S. (2010). Accelerating uplift in the North Atlantic region as an indicator of ice loss. *Nature Geoscience*, *3*(6), 404–407. https://doi.org/10.1038/ngeo845

Kümpel, H. J., Peters, J. A., & Bower, D. R. (1988). Nontidal tilt and water table variations in a seismically active region in Quebec, Canada. *Tectonophysics*, *152*(3–4), 253–265. https://doi.org/10.1016/0040-1951(88)90051-0

Lagler, K., Schindelegger, M., Böhm, J., Krásná, H., & Nilsson, T. (2013). GPT2: Empirical slant delay model for radio space geodetic techniques. *Geophysical Research Letters*, *40*, 1069–1073. https://doi.org/10.1002/grl.50288

Lin, L. I.-K. (1989). A concordance correlation coefficient to evaluate reproducibility. *Biometrics*, *45*(1), 255–268. https://doi.org/10.2307/2532051

Lin, L. I.-K. (2000). Correction: A note on the concordance correlation coefficient. *Biometrics*, *56*(1), 324–325.

Longuevergne, L., Florsch, N., Boudin, F., Oudin, L., & Camerlynck, C. (2009). Tilt and strain deformation induced by hydrologically active natural fractures: Application to the tiltmeters installed in Sainte-Croix-aux-Mines observatory (France). *Geophysical Journal International*, *178*(2), 667–677. https://doi.org/10.1111/j.1365-246X.2009.04197.x

Lyard, F., Lefevre, F., Letellier, T., & Francis, O. (2006). Modelling the global ocean tides: Modern insights from FES2004. *Ocean Dynamics*, *56*(5-6), 394–415. https://doi.org/10.1007/s10236-006-0086-x

Maillet, E. (1905). *Essais D'hydraulique Souterraine Et Fluviale*, *Librairie Sci.* (p. 218). Paris: A. Hermann.

Mietto, P., & Sauro, U. (2000). *Grotte del Veneto. Paesaggi Carsici e Grotte del Veneto* (p. 480). Vago di Lavagno: Editrice La Grafica.

Milanović, P. (1981). *Karst hydrogeology* (p. 434). Littleton, Colo: Water Resources Publication.

Milanović, P. (2005). Water resources engineering in karst. *Choice Reviews Online*, *42*(5), 42-2822. https://doi.org/10.5860/choice.42-2822
Milanović, P. (2014). Hydraulic properties of karst groundwater and its impacts on large structures. In J. Mudry, F. Zwahlen, C. Bertrand, & J. W. LaMoreaux (Eds.), *H2Karst Research in Limestone Hydrogeology* (pp. 19–48). Cham: Springer International Publishing. https://doi.org/10.1007/978-3-319-06139-9_2
Moreau, F., & Dauteuil, O. (2013). Geodetic tools for hydrogeological surveys: 3D-displacements above a fractured aquifer from GPS time series. *Engineering Geology*, *152*(1), 1–9. https://doi.org/10.1016/j.enggeo.2012.10.017
Okada, Y. (1985). Surface deformation to shear and tensile faults in a halfspace. *Bulletin of the Seismological Society of America*, *75*, 1135–1154.
Petrie, E. J., King, M. A., Moore, P., & Lavallée, D. A. (2010). Higher-order ionospheric effects on the GPS reference frame and velocities. *Journal of Geophysical Research*, *115*, B03417. https://doi.org/10.1029/2009JB006677
Rahnama, M., & Gloaguen, R. (2014a). TecLines: A MATLAB-based toolbox for tectonic lineament analysis from satellite images and DEMs, Part 1: Line segment detection and extraction. *Remote Sensing*, *6*(7), 5938–5958. https://doi.org/10.3390/rs6075938
Rahnama, M., & Gloaguen, R. (2014b). TecLines: A MATLAB-based toolbox for tectonic lineament analysis from satellite images and DEMs, Part 2: Line segments linking and merging. *Remote Sensing*, *6*(11), 11,468–11,493. https://doi.org/10.3390/rs61111468
Ramsay, J. G., & Huber, M. I. (1983). *The Techniques of Modern Structural Geology. Volume 1: Strain. Analysis* (307 pp.). London: Academic Press.
Rodell, M., Houser, P. R., Jambor, U., Gottschalck, J., Mitchell, K., Meng, C., et al. (2004) The Global Land Data Assimilation System. *Bulletin of the American Meteorological Society*, *85*, 381–394. https://doi.org/10.1175/BAMS-85-3-381
Sauter, M. (1992). Quantification and forecasting of regional groundwater flow and transport in a karst aquifer (Gallusquelle, Malm, SW. Germany). Tübinger Geowissenschaftliche Arbeiten C13, Tübingen.
Schmid, R., Rothacher, M., Thaller, D., & Steigenberger, P. (2005). Absolute phase center corrections of satellite and receiver antennas. *GPS Solutions*, *9*(4), 283–293. https://doi.org/10.1007/s10291-005-0134-x
Schmid, R., Steigenberger, P., Gendt, G., Ge, M., & Rothacher, M. (2007). Generation of a consistent absolute phase-center correction model for GPS receiver and satellite antennas. *Journal of Geodesy*, *81*(12), 781–798. https://doi.org/10.1007/s00190-007-0148-y
Schmid, S. M., Bernoulli, D., Fügenschuh, B., Matenco, L., Schefer, S., Schuster, R., Tischler, M., & Ustaszewski, K. (2008). The Alpine-Carpathian-Dinaridic orogenic system: correlation and evolution of tectonic units. *Swiss Journal of Geosciences*, *101*(1), 139–183. https://doi.org/10.1007/s00015-008-1247-3
Schmidt, S., Geyer, T., Guttman, J., Marei, A., Ries, F., & Sauter, M. (2014). Characterisation and modelling of conduit restricted karst aquifers—Example of the Auja spring, Jordan Valley. *Journal of Hydrology*, *511*, 750–763. https://doi.org/10.1016/j.jhydrol.2014.02.019
Schuite, J., Longuevergne, L., Bour, O., Boudin, F., Durand, S., & Lavenant, N. (2015). Inferring field-scale properties of a fractured aquifer from ground surface deformation during a well test. *Geophysical Research Letters*, *42*, 10,696–10,703. https://doi.org/10.1002/2015GL066387
Serpelloni, E., Casula, G., Galvani, A., Anzidei, M., & Baldi, P. (2006). Data analysis of permanent GPS networks in Italy and surrounding regions: Application of a distributed processing approach. *Annales Geophysique*, *49*, 897–928. https://doi.org/10.4401/ag-4410
Serpelloni, E., Faccenna, C., Spada, G., Dong, D., & Williams, S. D. P. (2013). Vertical GPS ground motion rates in the Euro-Mediterranean region: New evidence of velocity gradients at different spatial scales along the Nubia-Eurasia plate boundary. *Journal of Geophysical Research: Solid Earth*, *118*, 6003–6024. https://doi.org/10.1002/2013JB010102
Serpelloni, E., Vannucci, G., Anderlini, L., & Bennett, R. A. (2016). Kinematics, seismotectonics and seismic potential of the eastern sector of the European Alps from GPS and seismic deformation data. *Tectonophysics*, *688*, 157–181. https://doi.org/10.1016/j.tecto.2016.09.026
Silverii, F., D'Agostino, N., & Métois, M. (2016). Transient deformation of karst aquifers due to seasonal and multiyear groundwater variations observed by GPS in southern Apennines (Italy). *Journal of Geophysical Research: Solid Earth*, *121*, 8315–8337. https://doi.org/10.1002/2016JB013361
Sitharam, T. G., Sridevi, J., & Shimizu, N. (2001). Practical equivalent continuum characterization of jointed rock masses. *International Journal of Rock Mechanics and Mining Sciences*, *38*(3), 437–448. https://doi.org/10.1016/S1365-1609(01)00010-7
Swenson, S., Chambers, D., & Wahr, J. (2008). Estimating geocenter variations from a combination of GRACE and ocean model output. *Journal of Geophysical Research*, *113*, B08410. https://doi.org/10.1029/2007JB005338
Takemoto, S. (1995). Recent results obtained from continuous monitoring of crustal deformation. *Journal of Physics of the Earth*, *43*(4), 407–420. https://doi.org/10.4294/jpe1952.43.407
Tregoning, P., & van Dam, T. (2005). Atmospheric pressure loading corrections applied to GPS data at the observation level. *Geophysical Research Letters*, *32*, L22310. https://doi.org/10.1029/2005GL024104
van Dam, T. M., Blewitt, G., & Heflin, M. B. (1994). Atmospheric pressure loading effects on global positioning system coordinate determinations. *Journal of Geophysical Research*, *99*(B12), 23,939–23,950. https://doi.org/10.1029/94JB02122
Villagra, M. M., Bacchi, O., Tuon, R. L., & Reichardt, K. (1995). Difficulties of estimating evapotranspiration from the water-balance equation. *Agricultural and Forest Meteorology*, *72*(3–4), 317–325. https://doi.org/10.1016/0168-1923(94)02168-J
Wahr, J., Khan, S. A., van Dam, T., Liu, L., van Angelen, J. H., van den Broeke, M. R., & Meertens, C. M. (2013). The use of GPS horizontals for loading studies, with applications to northern California and southeast Greenland. *Journal of Geophysical Research: Solid Earth*, *118*, 1795–1806. https://doi.org/10.1002/jgrb.50104
Wessel, P., Smith, W. H. F., Scharroo, R., Luis, J. F., & Wobbe, F. (2013). Generic mapping tools: Improved version released. *Eos, Transactions American Geophysical Union*, *94*(45), 409–410. https://doi.org/10.1002/2013EO450001